

A Multiphysics Modeling Approach to Assess the Powder Bed Characteristics of High Strength Steel in Selective Laser Melting

M. Rangapuram¹, M. Yang¹, S. Babalola², J. W. Newkirk², L. N. Bartlett², F. F. Liou¹, and K. Chandrashekhara¹

¹Department of Mechanical and Aerospace Engineering

²Department of Materials Science and Engineering

Missouri University of Science and Technology, Rolla, MO 65409

Abstract:

Selective laser melting (SLM) is a type of additive manufacturing technique which uses a powder bed to form complex metal parts in a layer-by-layer process. The density of the powder bed in SLM affects the mechanical properties of the produced part. Good powder packing results in a higher powder bed density which in turn influences the quality of the produced part. In this work, a computational fluid dynamics (CFD) model was developed for the SLM process using Flow 3D software to study the effect of powder bed density on the melt pool characteristics of high strength steel. Discrete element method (DEM) was used to generate powder beds with realistic powder properties. The realistic powder properties of AF9628 were obtained using JMatPro software. The powder beds were irradiated with a moving laser heat source to study the melt pool characteristics. These models were validated with experimental results.

1. Introduction

Additive manufacturing (AM) is defined as “the process of joining materials to make objects from three-dimensional model data” by American Society for Testing and Materials (ASTM) [1]. Complex geometries can be easily manufactured compared to conventional subtractive methods with more freedom and flexibility in the design process. This method has revolutionized the way parts are manufactured which reduces the overall weight, facilities and materials used [2]. Powder bed additive manufacturing is a subset of additive manufacturing techniques which uses powder as a feed stock material. Laser Powder Bed Fusion (L-BPF) process selectively melts powder that is uniformly spread in a confined region. This method can produce parts that are utilized in aerospace, automotive, medical, and other fields [3-6]. As the demand for L-BPF process increased, it has become critical to understand the powder characteristics as it can adversely affect the quality of the parts produced. Several studies reported that the powder properties namely uniformity and packing density affect the final porosity and bulk density of the manufactured part [5,7,8]. The machine parameters and powder characteristics affect the layer uniformity and density of the powder bed [9]. Through L-BPF process it is possible to manufacture complex shapes by melting powder bed with a high energy laser. However, this may be inconceivable for traditional manufacturing methods [10].

There are various strategies to model L-BPF process including from part scale to particle scale. This ranges from part scale or macroscopic models to mesoscopic and microscopic models [11-13]. The thermal behavior, flow behavior is often predicted using mesoscopic models. The part

scale models are generally utilized to predict and understand temperature distribution and residual stresses in the parts [14-16]. In this work, a mesoscopic model based on FDM (Finite Difference Method) was developed to simulate the thermal and flow behavior of high strength steel AF9628 in a powder bed system. The DEM (Discrete Element Method) was used to generate randomly packed powder bed with realistic powder size distributions. The free surface evolution was captured using VOF (Volume of Fluid) method. The modeling efforts were compared with experimental results.

2. Numerical Model

The L-BPF process is a complex process involving various thermo-physical processes like conduction, convection, radiation heat transfer, melting, evaporation and solidification. To simplify the model and to make the models computationally inexpensive several assumptions are made to simplify the process: 1) The powder particles are spatially fixed after powder bed extraction, and they don't move during laser material interaction. 2) Except specific heat, conductivity, viscosity, and surface tension some of the properties are considered temperature independent for simplification. A commercial CFD software Flow-3D was used for modeling in this study. Flow-3D is based on volume of fluid method. The software is capable of modeling free surface flows with integrated multi-physics capabilities. This software is capable of effectively modeling particle-particle interactions and generating powder beds using DEM. The beds generated were then solved for thermal behavior and melt morphology.

2.1 Generating randomly packed powder bed

A discrete element model was developed with realistic powder properties. This model was used to simulate the complex processes in SLM like settling and spreading. This model could predict the powder bed density and factors that can affect the powder bed density.

2.1.1 Discrete Element Method: Discrete element method (DEM) is an effective way to analyze the impact motion of many solid elements mainly particulate materials. It can be applied to a variety of applications in combination with flow analysis. The particle-particle collisions are modeled using Voight model in which the force between two particles upon collision is evaluated using a combination of spring and a damper. The spring captures the force related to deformation and the damper captures the force related to relative velocity upon collision in other words known as viscous damping. For Voight model the spring and the damper are connected in parallel. The force is divided into components in normal and tangential direction. To calculate the contact force the material properties must be condensed in a spring coefficient and viscous damping coefficient. Additional material properties required to model are discussed in table 1. The fundamental equation for DEM and Voight model is presented below.

$$m_i a_i = \sum F_c + g \quad (1)$$

Where m_i is the mass of the solid particle, a_i is the acceleration of the solid particles, F_c is the contact force due to particle interaction and g is the external force and gravity.

$$\varepsilon_{Total} = \varepsilon_{Spring} = \varepsilon_{Damper} \quad (2)$$

$$\sigma_{Total} = \sigma_{Spring} + \sigma_{Damper} \quad (3)$$

Where σ is the stress and ε is the strain.



Figure 1. (a) Representation of particle-particle interactions (b) Voigt model

2.2 Conservation equations:

The melt flow inside the melt pool is governed by Navier-Stokes equations. The free surface was captured using VOF method. Fractional Area/Volume Obstacle Representation (FAVOR) method was used to deal with dynamic boundary problems. The Flow 3D utilized the following set of equations to solve the conservation of mass, momentum, and energy.

$$\text{Mass: } \frac{\partial u}{\partial t} + \frac{\partial(\rho u)}{\partial x} + \frac{\partial(\rho v)}{\partial y} + \frac{\partial(\rho w)}{\partial z} = 0 \quad (4)$$

$$\text{Momentum: } \frac{\partial \vec{V}}{\partial t} + (\vec{V} \cdot \nabla) \vec{V} = -\frac{1}{\rho} \nabla P + \mu \nabla^2 \vec{V} + \vec{g}[1 - \beta(T - T_m)] \quad (5)$$

$$\text{Energy: } \frac{\partial H}{\partial t} + (\vec{V} \cdot \nabla) H = \frac{1}{\rho} (\nabla \cdot k \nabla T) + S_U \quad (6)$$

Where ρ is the liquid density, u , v , and w represent the components of the velocity vector along X, Y, and Z axes, respectively, \vec{V} represents velocity of the melt metal liquid, P represents hydrodynamic pressure, μ represents liquid viscosity, \vec{g} represents the gravitational acceleration, β represents volumetric thermal expansion coefficient of the material, T represents the fluid temperature, T_m represents the melting temperature, k is the thermal conductivity, S_U is the energy source term, and H is the enthalpy which is considered to be a linear function of temperature T , depending on the solid fraction of the fluid.

The VOF method was employed to track the free surface evolution of the particles as they melted into the melt pool, and it defined a function of the fraction of fluid as the following equation.

$$\frac{\partial F}{\partial t} + \nabla \cdot (\vec{V} F) = 0 \quad (7)$$

where F represents the fluid volume fraction within the cell. $F=1$, when the cell is full of fluid, $F=0$, when it is void. The value is between 0 and 1 when the void and fluid coexist in a cell.

2.2.1 Realistic Powder Properties for Powder Bed Generation: The AF9628 powder was analyzed using ASPEX SEM. The particle size distribution details can be found in figure 2. 80% of the powder particles are below 25 μm . 20% of the particles were between 25-80 μm . This realistic particle size distribution was used as input parameter to generate the powder beds using DEM model. The properties listed in table 1 were used for simulating the powder beds in this study.

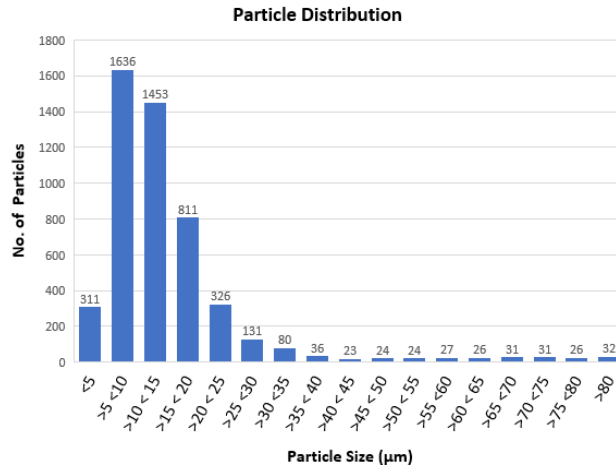


Figure 2. Realistic particle size distribution of AF9628

Table 1. List of properties required for modeling

Property	Value
Coef. of static friction	0.2
Coef. of dynamic friction	0.15
Coef. of restitution	0.3
Density	7 (g/cm^3)
Spring constant	20
Spreader velocity	0.125 (cm/s)
Layer thickness	60 μm

2.3 Powder Bed Generation: The powder delivery process in a typical SLM process will follow a powder settling step where the powder is delivered on the build plate through a hopper. This delivered powder is then uniformly spread across the build plate using a powder spreading process. The powder spreading process generally helps in powder compaction, achieving the prescribed layer thickness and generating a dense powder bed. The steps in a typical powder spreading process can be found in figure 3. We can see the particles have been initially settled on powder bed and then a spreader uniformly spreads the powder across the powder bed generating a compact powder bed achieving the predetermined layer height.

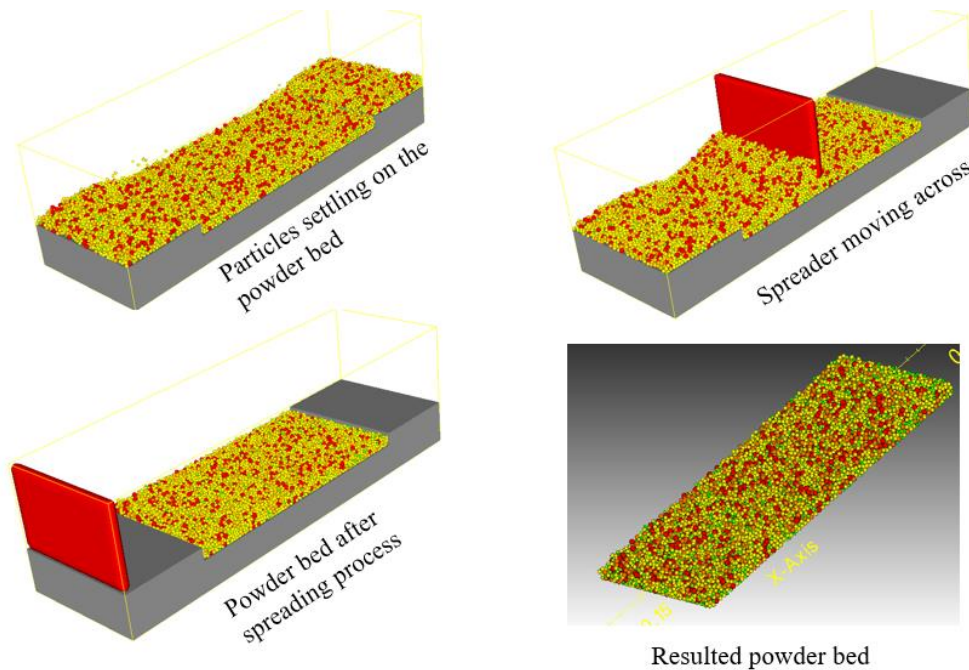


Figure 3. Schematic illustrating various steps in powder bed generation

2.4 Material physical properties

To simulate the SLM process, the thermophysical properties of AF9628 have been obtained using JMatPro software. The properties used in the simulation are listed in table 2 and figure 4. The laser parameters used in the simulation can be found in table 3.

Table 2. AF9628 material properties

Parameter	Value	Units
Ratio of specific heat	1.4	No units
Liquidus temperature**	1763.5	K
Solidus temperature**	1713.15	K
Accommodation coefficient	0.005	No units
Latent heat of fusion*	2.77E+09	erg/g
Heat transfer coefficient*	1.0E10	erg/s/cm ² /K
Latent heat of vaporization*	6.3E010	cm ² /s ²
Saturation pressure*	1E06	g/cm s ²
Saturation temperature*	2500	K
Vapor specific heat*	6E06	cm ² /s ² K

Where * Values taken from literature and ** Values obtained from JMatPro (Missouri S&T)

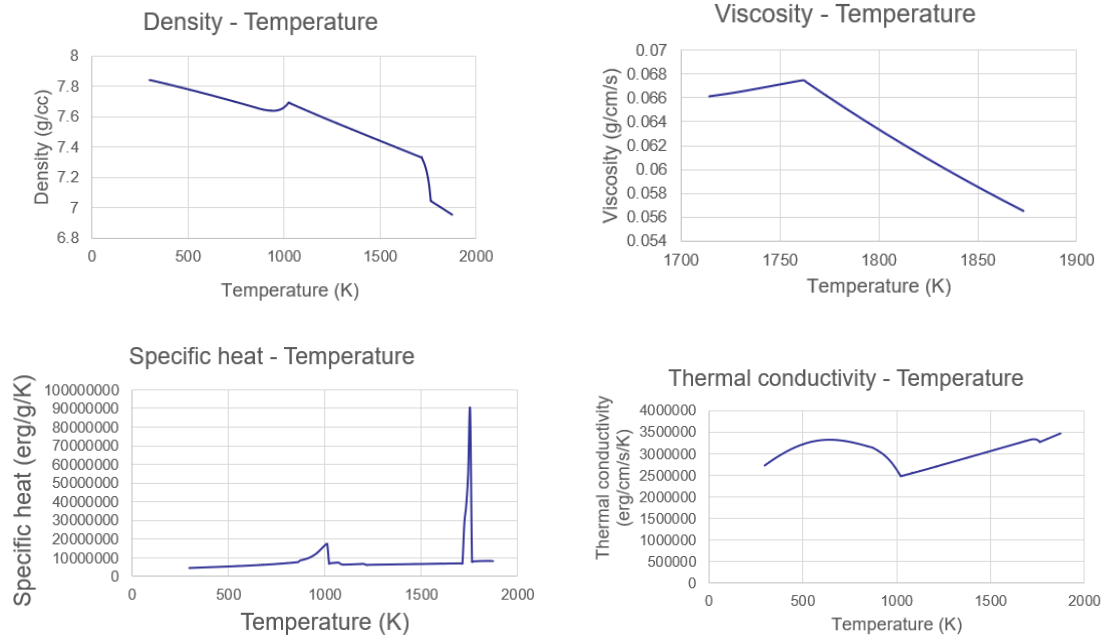


Figure 4. Temperature dependent thermophysical properties of AF9628 obtained from JMatPro

Table 3. Laser parameters used in the model

Parameter	Value
Laser power	125 & 75 W
Scan speed	60 & 55 cm/sec
Laser spot size	150 μm
Focal distance	0.978 cm

2.5 Laser Material Interaction Model: A typical SLM process includes steps like powder settling, powder spreading and laser material interaction. A schematic of SLM process is shown in figure 5. The powder bed generated using realistic particle size distribution is extracted and meshed to be used in laser material interaction. A meso-scale CFD model was developed to study the laser material interaction on the powder bed. The laser material interaction is a complex phenomenon which requires to capture various physics involved in it. The material properties required to model laser material interaction are listed in table 2. For laser material interaction temperature dependent physical properties of AF9628 like density, viscosity, specific heat, and thermal conductivity were obtained using JMatPro. The temperature dependent properties can be found in figure 4.

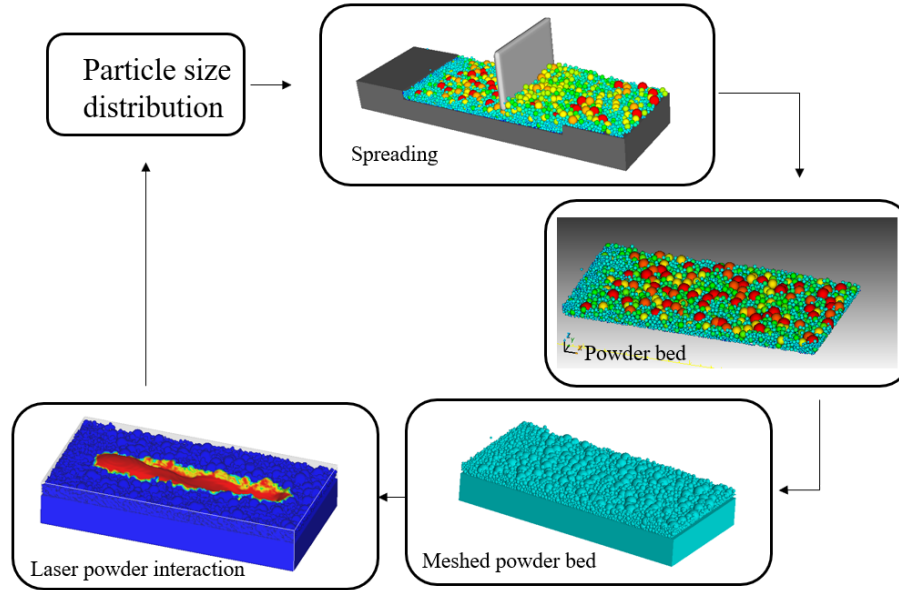


Figure 5. Schematic of SLM process

2.5.1 Laser properties: The initial conditions and the laser parameters of the model setup are listed in table 4 and table 5. The trial model was simulated to run time of 0.002 seconds.

Table 4. Initial conditions of the model

Boundary	Type
X-Min	Wall at 293 K, Heat transfer coefficient 1.0E+05 erg/s/cm ² /K
X-Max	Wall at 293 K, Heat transfer coefficient 1.0E+05 erg/s/cm ² /K
Y-Min	Wall at 293 K, Heat transfer coefficient 1.0E+05 erg/s/cm ² /K
Y-Max	Wall at 293 K, Heat transfer coefficient 1.0E+05 erg/s/cm ² /K
Z-Min	Wall at 293 K, Heat transfer coefficient 1.0E+05 erg/s/cm ² /K
Z-Max	Pressure of 1.0e+05 dyne/cm ² (1.0e+04 N/m ²)

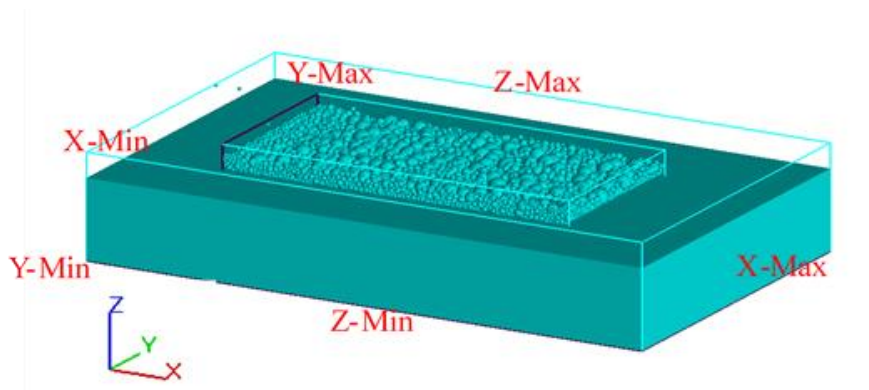


Figure 6. Xactmetal XM200C laser material interaction model

Table 5. Experimental Runs

Experimental Run	Laser Power (W)	Scan Speed (mm/s)
ER1	125	600
ER2	125	550
ER3	75	600
ER4	75	550

ER – Experimental Run

3. Results and Discussion

The experimental runs that have been modeled in Flow-3D have been analyzed to measure the dimensions of the melt pool after simulating a single track on the generated powder bed. The corresponding melt pool depths and widths have been measured in the models with the change in laser power and scan speeds.

3.1 Experimental run 1: Laser power of 125 W and scan speed of 600 mm/s was used in this run. The cross-section of the single-track melt pool can be found in figure 7. The figure shows the time history of the melt region during the simulation. The red region was completely melted during the laser interaction and solidified at the end of the simulation.

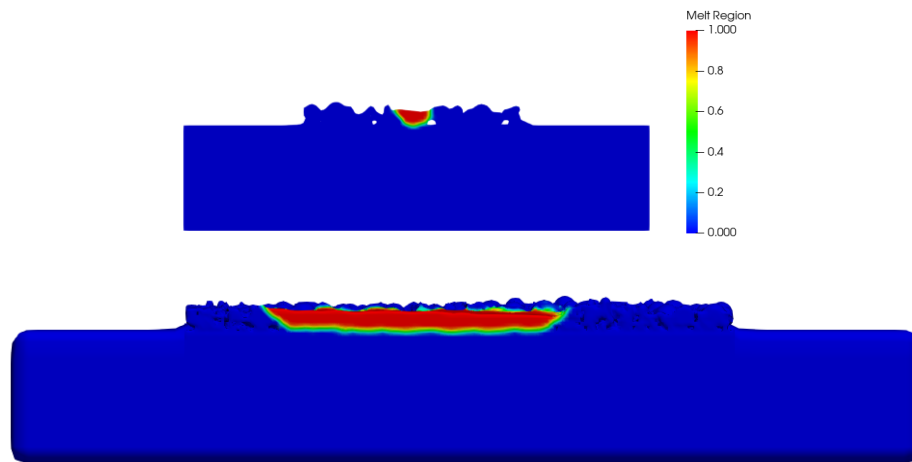


Figure 7. The cross section of single-track melt pool (ER1)

3.1.1 Validation: The experimental deposition was performed using Xactmetal XM 200C machine with the same parameters as ER1 (125 W laser power and 600 mm/s scan speed). The deposit was then cut using high pressure waterjet cutting to obtain a sample to perform microscopy. The obtained samples were then etched using 4% Nigalex solution for 90 seconds and 4% Nital. The

specimen was then examined under optical microscope to obtain the micrographs with distinguishable melt pools. From the micrograph, perfect single tracks right above the substrate were identified and the melt pool depths and widths were measured using Image J. The average value of the melt pool depths and widths have been reported. In figure 8, the optical micrograph with single tracks can be seen and the dimensions of the melt pool from model as well as the average values from the experimental deposition can be found.

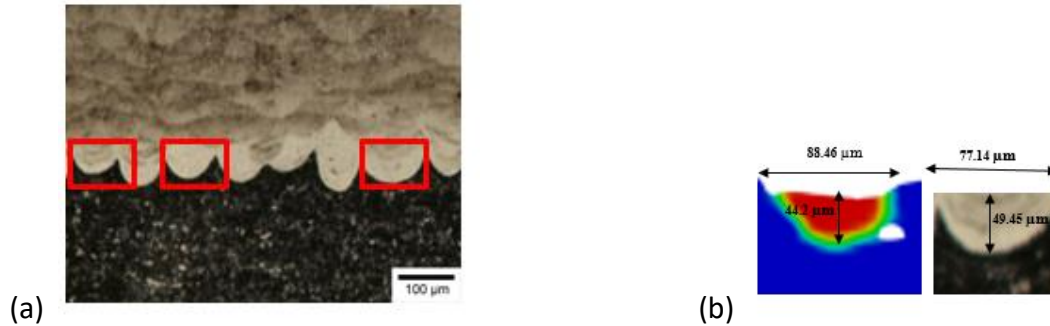


Figure 8. (a) Optical micrograph of the printed specimen (b) The melt pool depths and widths from model and the experimental deposition

3.2 Experimental run 2: Laser power of 125 W and scan speed of 550 mm/s was used in this run. The cross-section of the single-track melt pool can be found in figure 9 (a). The melt pool depth and width from the model and the experimental deposition can be found in figure 9 (b).

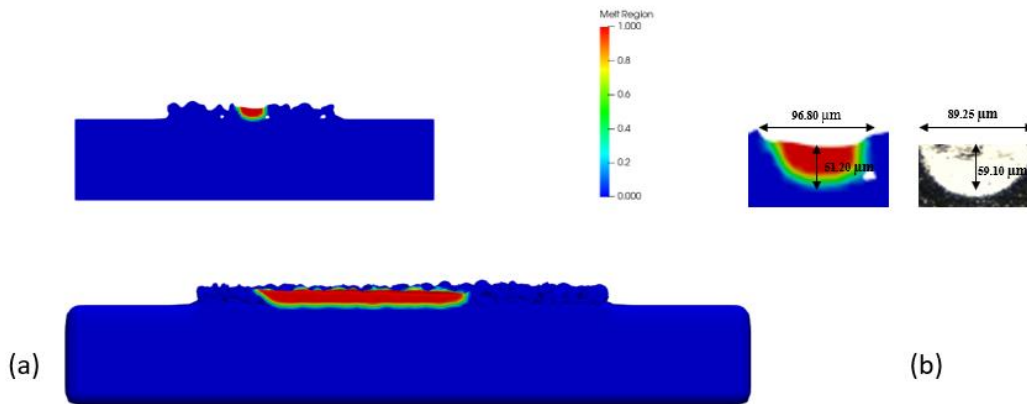


Figure 9. (a) The cross section of single-track melt pool (ER2) (b) The melt pool depths and widths from model and the experimental deposition

3.3 Experimental run 3: Laser power of 75 W and scan speed of 600 mm/s was used in this run. The cross-section of the single-track melt pool can be found in figure 10 (a). The melt pool depth and width from the model and the experimental deposition can be found in figure 10 (b).

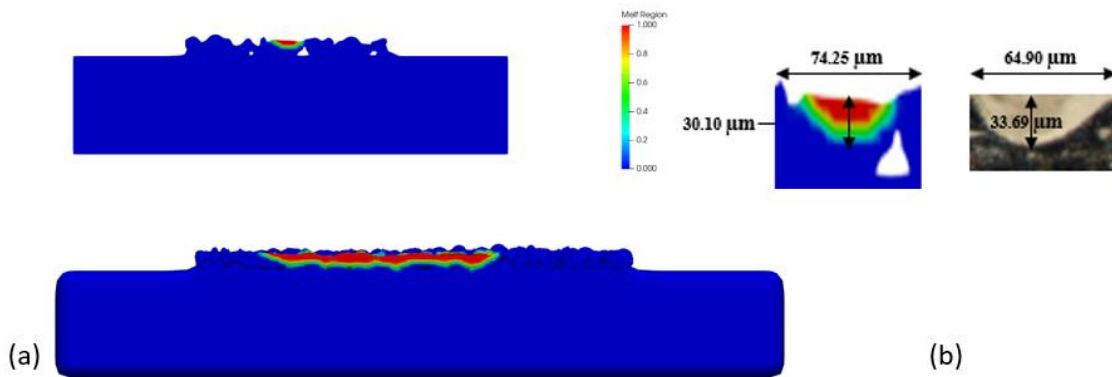


Figure 10. (a) The cross section of single-track melt pool (ER3) (b) The melt pool depths and widths from model and the experimental deposition

3.4 Experimental run 4: Laser power of 75 W and scan speed of 550 mm/s was used in this run. The cross-section of the single-track melt pool can be found in figure 11 (a). The melt pool depth and width from the model and the experimental deposition can be found in figure 11 (b).

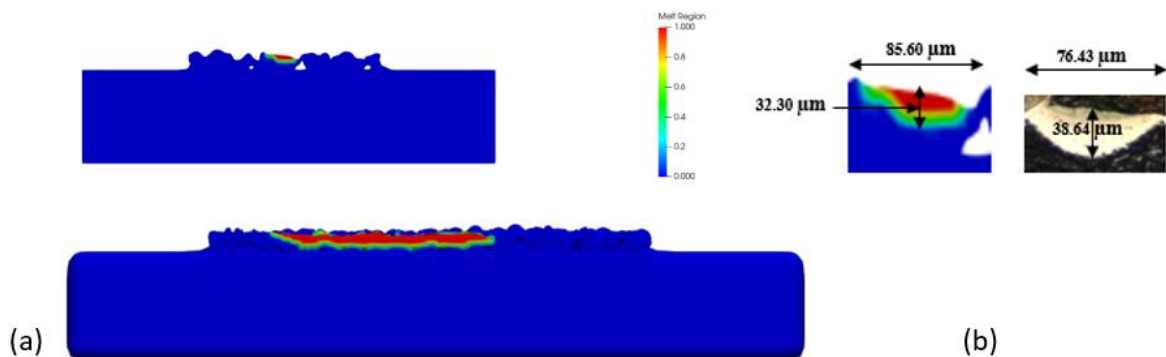


Figure 11. (a) The cross section of single-track melt pool (ER4) (b) The melt pool depths and widths from model and the experimental deposition

From the models it was evident that at constant laser power of 125 W, the scan speed was affecting the melt pool dimensions. The slower scan speed resulted in increased depths and widths, whereas the increased scan speed resulted in relatively smaller melt pool depths and widths. Similar trend was observed in 75 W models, the slower scan speed of 550 mm/s resulted in higher melt pool depths and widths than the faster scan speed of 600 mm/s. The 125 W models namely ER1 and ER2 were completely melting the layer (figure 10 (a) and figure 11 (a)). From the ER3 and ER4

models it was evident that the laser power was not completely melting the layer (figure 10 (a) and figure 11 (a)). The complete dimensions of the melt pools from all the cases can be found in table 6.

Table 6. Comparison of melt pool dimensions from model with experimental run

	Model	Experiment		Model	Experiment	
Experimental Run	Melt pool depth (μm)	Melt pool depth (μm)	Error (%)	Melt pool width (μm)	Melt pool width (μm)	Error (%)
ER1	44.2	49.45	10.62	88.46	77.14	14.67
ER2	51.20	59.10	13.37	96.80	89.25	8.46
ER3	30.10	33.69	10.65	74.25	64.90	14.40
ER4	32.30	38.64	16.40	85.60	76.43	12.00

4. Summary and conclusion

In summary, powder beds with realistic powder properties were generated using DEM method. The generated powder beds were irradiated with a moving laser heat source to study the melt pool dimensions to understand the effect of laser power and scan speed. Experimental validation was performed using Xactmetal XM200C machine. Both the models and experiments indicated that, with the increase in scan speed the melt pool dimensions decreased. With the increase in laser power the melt pool dimensions correspondingly increased. At constant laser power, the scan speed affects the melt pool dimensions and vice versa. The 75 W models showed the formation of lack of fusion defects indicating the laser power was not sufficient for the layer to melt completely.

5. Acknowledgment

This project is supported from the DEVCOM Army Research Laboratory (Cooperative Agreement Number W911NF-20-2-0251). The views and conclusions contained in this document are those of the authors and should not be interpreted as representing the official policies, either expressed or implied, of the DEVCOM Army Research Laboratory or the U.S. Government. The U.S. Government is authorized to reproduce and distribute reprints for Government purposes, notwithstanding any copyright notation herein. The authors would like to thank Dr. Stephen Cluff for his insightful suggestions for this project.

References:

1. ASTM, ASTM F2792-12a: Standard Terminology for Additive Manufacturing Technologies, ASTM International, West Conshohocken, PA, 2012.
2. P. Markillie, A third industrial revolution. *The Economist* 21 (2012). <https://www.economist.com/node/21552901>.
3. D. Wang, Z.Y. Qian, and W.H. Dou, "Research Progress on selective laser melting of nickel-based superalloy," *Aeronautical Manufacturing Technology*, Volume 61, Pages 49–60, 2018.
4. B. Vandenbroucke, and J.P. Kruth, "Selective laser melting of biocompatible metals for rapid manufacturing of medical parts," *Rapid Prototyping Journal*, Volume 13, Pages 196-203, 2007.
5. D. Herzog, V. Seyda, E. Wycisk, and C. Emmelmann, "Additive manufacturing of metals," *Acta Materialia*, Volume 117, Pages 371-392, 2016.
6. G. Yablokova, M. Speirs, J. Van Humbeeck, J.-P. Kruth, J. Schrooten, R. Cloots, F. Boschini, G. Lumay, and J. Luyten, "Rheological behavior of β -Ti and NiTi powders produced by atomization for SLM production of open porous orthopedic implants," *Powder Technology*, Volume 283, Pages 199-209, 2015.
7. X. Gong, T. Anderson, and K. Chou, "Review on powder-based electron beam additive manufacturing technology," *Manufacturing Review*, Volume 1, Pages 1-12, 2014.
8. J. Dawes, R. Bowerman, and R. Trepleton, "Introduction to the additive manufacturing powder metallurgy supply chain," *Johnson Matthey Technology Review*, Volume 59, Pages 243–256, 2015.
9. A.B. Spierings, M. Voegtlin, T. Bauer, and K. Wegener, "Powder flowability characterization methodology for powder-bed-based metal additive manufacturing," *Progress in Additive Manufacturing*, Volume 1, Pages 9-20, 2016.
10. D. D. Gu, W. Meiners, K. Wissenbach, and R. Poprawe, "Laser additive manufacturing of metallic components: materials, processes and mechanisms," *International Materials Reviews*, Volume 57, Pages 133-164, 2012. (DOI: 10.1179/1743280411Y.0000000014)
11. C. Meier, R.W. Penny, Y. Zou, J. S. Gibbs, and A. J. Hart, "Thermophysical Phenomena in Metal Additive Manufacturing by Selective Laser Melting: Fundamentals, modeling, Simulation and Experimentation," *Annual Review of Heat Transfer*, Volume 20, Pages 241-316, 2017. (<https://arxiv.org/abs/1709.09510>)

12. W. J. Sames, F. A. List, S. Pannala, R. R. Dehoff, and S. S. Babu, "The metallurgy and processing science of metal additive manufacturing," *International Materials Reviews*, Volume 61, Pages 315-360, 2016. (DOI: 10.1080/09506608.2015.1116649)
13. W.E. King, A.T. Anderson, R.M. Ferencz, N. E. Hodge, C. Kamath, S. A. Khairallah, and A. M. Rubenchik, "Laser powder bed fusion additive manufacturing of metals; physics, computational, and materials challenges," *Applied Physics Reviews*, Volume 2, Issue 4, id.041304, 2015.
14. R.B. Patil, and V. Yadava, "Finite element analysis of temperature distribution in single metallic powder layer during metal laser sintering," *International Journal of Machine Tools and Manufacture*, Volume 47, Pages 1069–1080, 2007.
15. A. Foroozmehr, M. Badrossamay, E. Foroozmehr, and S. Golabi, "Finite Element Simulation of Selective Laser Melting process considering Optical Penetration Depth of laser in powder bed," *Materials & Design*, Volume 89, Pages 255-263, 2016
16. A. Hussein, L. Hao, C. Yan, and R. Everson, "Finite element simulation of the temperature and stress fields in single layers built without-support in selective laser melting," *Materials & Design (1980-2015)*, Volume 52, Pages 638-647, 2013.